MnO_2-decorated N-doped carbon nanotube with boosted activity for low-temperature oxidation of formaldehyde

Shuai Peng[b], Xixian Yang[a*], James Strong[c], Binoy Sarkar[d], Qiang Jiang[e], Feng Peng[f], Defei Liu[a], Hailong Wang[g,h]**

[a] School of Environmental and Chemical Engineering, Foshan University, Foshan, 528000, China

[b] Hubei Provincial Engineering Laboratory for Clean Production and High Value Utilization of Bio-Based Textile Materials, Wuhan Textile University, Wuhan, 430073, China

[c] School of Biology and Environmental Science, Centre for Agriculture and the Bioeconomy, Queensland University of Technology, GPO Box 2432, 2 George St, Brisbane, QLD 4001, Australia

[d] Lancaster Environment Centre, Lancaster University, Lancaster, LA1 4YQ, UK

[e] School of Chemistry and Chemical Engineering, South China University of Technology, Guangzhou, 510000, China

[f] School of Chemistry and Chemical Engineering, Guangzhou University, Guangzhou, 510000, China

[g] Biochar Engineering Technology Research Center of Guangdong Province, Foshan University, Foshan, Guangdong 528000, China

[h] Key Laboratory of Soil Contamination Bioremediation of Zhejiang Province, Zhejiang A&F University, Hangzhou, Zhejiang 311300, China

*Corresponding authors:

Xixian Yang Email: yangxixian@yeah.net Tel/Fax: +86 757 82272751

**Corresponding author:

Hailong Wang Email: hailong.wang@fosu.edu.cn Tel/Fax: +86 757 82272751

Highlights

- A simple *in-situ* oxidation approach was developed to prepare MnO_2/NCNT.
- Prepared samples showed boosted activity for HCHO degradation at low temperature.
- MnO_2/NCNT exhibited better activity and selectivity than MnO_2/CNT.
- Mechanism of improved HCHO oxidation by MnO_2/NCNT was revealed.

Graphical Abstract

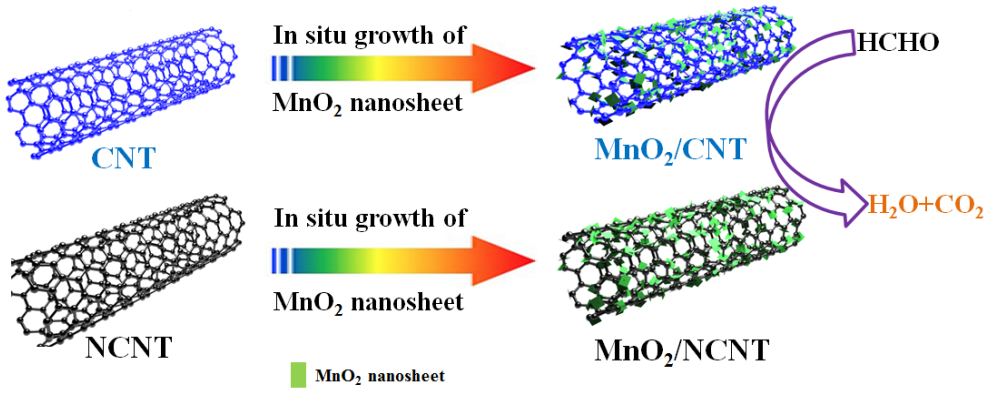

Abstract: Low-temperature oxidative degradation of formaldehyde (HCHO) using non-noble metal catalysts is challenging. Herein, novel manganese dioxide (MnO_2)/N-doped carbon nanotubes (NCNT) composites were prepared with varying MnO_2 content. The surface properties and morphologies were analyzed using X-ray photoelectron spectroscopy (XPS), scanning electron microscope (SEM) and transmission electron microscope (TEM). Comparing with MnO_2/carbon nanotubes (CNTs) catalyst, the 40% MnO_2/NCNT exhibited much better activity and selectivity for HCHO oxidation, mineralizing 95% of HCHO (at 100 ppm) into CO_2 at 30 °C at a gas hourly space velocity (GHSV) of 30,000 mL h^{-1} g^{-1}. Density functional theory (DFT) calculation was used to analyze the difference in the catalytic activity of MnO_2 with CNTs and NCNT carrier. It was confirmed that the oxygen on NCNT was more active than CNTs, which facilitated the regeneration of MnO_2. This resulted in remarkably boosted activity for HCHO oxidation. The present work thus exploited an inexpensive approach to enhance the catalytic activity of transition metal oxides *via* depositing them on a suitable support.

Keywords: Manganese dioxide; carbon nanotube; low-temperature; catalytic oxidation; formaldehyde removal

1. Introduction

In recent years, preventing or mitigating harmful volatile organic compound (VOC) emissions has been intensively researched because of the directly-implicated adverse health effects associated with these gaseous pollutants [1-4]. Formaldehyde (HCHO) is considered as one of the most harmful air pollutants in indoor environments. A chronical exposure to HCHO can lead to irreversible damage to skin, eyes and respiratory system, as well as can cause cerebrovascular diseases and cancers [5, 6]. Hence, the elimination of HCHO is essential for improving the safety of work or living environment.

To date, methods proposed for the removal of HCHO included adsorption [7, 8],

plasma oxidation [9-11], photocatalytic degradation [12-15], and catalytic oxidation [16-19]. Among these methods, catalytic oxidation has been considered to be a highly efficient approach to feasibly convert HCHO into CO_2 and H_2O under mild conditions [20]. Traditionally, noble metal catalysts (e.g., Pt, Pd, Au) were commonly used for low temperature oxidation of HCHO due to the high catalytic efficiency and selectivity. However, high cost and scarcity have limited their application [21-24]. Therefore, exploring cost-effective, alternative catalysts for the HCHO oxidation at low temperature or even at room temperature is highly demanded at the moment.

One of the most pragmatic strategies is to utilize supported transition metal oxides (e.g., Co_3O_4, CeO_2, TiO_2, MnO_2) as catalysts for the oxidation removal of HCHO ascribed to the inexpensive, adequate catalytic activity, and satisfactory thermal stability [25-27]. Manganese dioxide (MnO_2) is a practical choice for HCHO oxidation at room temperature [27]. It is regarded as the most active catalyst among transition metal oxides for HCHO oxidation because of its high oxidation-reduction potential. However, it remained a challenge to develop effective MnO_2-based catalysts for complete oxidation of HCHO at ambient temperatures with improved CO_2 selectivity [28].

Despite the challenges, various MnO_2 supported on carbon nanomaterials demonstrate excellent catalytic activity due to accelerated charge transport resulting from well-designed morphology and structure [29]. Both generic and heteroatom-doped carbon nanotube (CNT) has been meticulously tested for the above purposes in the last few years. N-doped carbon nanotube (NCNT) has become particularly appealing due to increased surface reactive sites improving catalytic performance [30]. Furthermore, a series of nanocomposite consisting of MnO_2 supported by NCNT have been widely applied, including as superior anodes for lithium ion batteries, cathodic catalysts for microbial fuel cells, electrodes for supercapacitors, and so on [30-32]. Unfortunately, most of the researches focusing on catalytic HCHO degradation investigated on the single component of MnO_2 or NCNT. As far as we know, there are no published reports with respect to well-dispersed MnO_2 nanosheets supported by NCNT for the low-

temperature catalytic removal of HCHO.

In this work, MnO_2 was directly deposited onto the NCNT surface using *in-situ* oxidation. The physical and chemical properties of MnO_2/NCNT were characterized. Subsequently, the MnO_2/NCNT composite was assessed for catalytic performance and selectivity. Compared with pure MnO_2 and MnO_2/CNT, the MnO_2/NCNT composite displayed higher activity and stability for the degradation of HCHO at lower temperature. Furthermore, density functional theory (DFT) calculations and x-ray photoelectron spectroscopy (XPS) analyses were verified that the combination of MnO_2 and NCNT had a strong synergistic catalytic effect *via* the formation of well-defined interfaces and improved interfacial electron transfer.

2. Experimental

2.1. Preparation of formaldehyde oxidation catalyst

Carbon nanotubes (CNTs) were synthesized according to our previous work [30]. The preparation details are contained in the Supporting Information.

N-doped carbon nanotubes (NCNT) were synthesized by a similar chemical vapor deposition (CVD) method as follows: 0.1 g Fe-Mo/Al_2O_3 catalyst (see reference [33]) was placed in a clean magnetic boat, which was placed in a quartz tube of a horizontal tube furnace with a 4 cm inner diameter and sealed. Ammonia (NH_3) gas was injected into the tube at a flowrate of 400 sccm over 10 min. The temperature was increased to 800 °C at a heating rate of 10 °C/min. Aniline (18 mL) was injected into the quartz tube at a rate of 3 mL/h *via* a microinjection pump. After 10 min, the furnace was turned off and the NH_3 flow rate lowered to100 sccm. When the furnace temperature dropped below 100 °C, NH_3 flow was replaced with air flushing at 500 sccm for 10 min. The sample was transferred into a stirred 30% nitric acid (HNO_3) solution for 10 min, followed by refluxing in an oil bath at 120 °C for 5 h. The mixture was diluted, filtered and thoroughly washed with deionized water until neutral. Finally, the filter cake was dried at 105 °C for 12 h to yield NCNTs.

The CNT modified MnO_2 catalysts (MnO_2/CNT) were prepared as follows: 500 mg CNTs was placed in 10 mL 5 wt % polyethylene glycol (average molecular weight 1000). After magnetic stirring for 1 h, deionized water was added and the suspension volume should reach to *x* mL. Then *y* g $KMnO_4$ was slowly added into the solution under stirring. This suspension was transferred into an oil bath, heated to 75 °C for 2 h under continuous magnetic stirring. After cooling to room temperature, the mixture was filtered, then washed with water and followed by exhaustive rinsing with ethanol for five times. The solid filter cake was dried in vacuum drying chamber at 80 °C for 12 hours to yield the MnO_2/CNTs catalysts. Different *x* and *y* content resulted in different MnO_2/CNT composites, as indicated below: When *x*=100 mL (40mL, 20mL), and *y*=1.7077 g (0.5667 g, 0.2214 g), MnO_2 content could reach to 70% (40%, 20%) and the catalyst was defined as 70 % MnO_2/CNTs (40% MnO_2/CNTs, 20% MnO_2/ CNTs).

The method described above was used to generate MnO_2/NCNT catalysts, also with 70% MnO_2/NCNT, 40% MnO_2/NCNT and 20% MnO_2/NCNT. All material was assessed for HCHO catalysis. The synthesis schematic illustration of MnO_2/NCNT was shown in Schematic.1.

2.2. Catalyst characterization

Scanning electron microscope (SEM) (LEO1530VP, Zeiss, Germany) and Transmission electron microscope (TEM) (JEM-2100F, JEOL, Japan) were used to observe the micro surface shape and structure of the catalyst. X-ray diffraction (XRD) analysis was carried out on a D8-Advance X-ray diffractometer with Cu- K_α radiation (λ=0.15418) (Bruker, Germany). Specific surface area of the catalysts was measured by N_2 adsorption tests performed on an ASAP-2010 analyzer (Micomeritics, USA) and calculated via Brunauer-Emmett and Teller (BET) method. X-ray photoelectron spectroscopy (XPS) was conducted using a Thermo ESCALAB 250Xi X-ray photoelectron spectrometer with Al K_α X-ray source (1486.7 eV, 10.8 mA and 30 kV).

2.3. Catalytic oxidation

Catalytic oxidation test was performed using a custom-designed HCHO removal

system (Fig. S1; Supporting Information). Different catalyst samples (0.2 g) were uniformly dispersed in a glass tube (i.d. = 6.0 mm, length = 9 mm). After the tube was fixed in the reactor, the stream containing approximately 100 parts per million (ppm) HCHO was generated from polyformaldehyde at a temperature of 0 °C. The HCHO and CO_2 concentrations (ppm) were analyzed by an Agilent 7890A online gas chromatograph with a flame ionization detector. The HCHO removal efficiency was calculated as:

HCHO removal efficiency (%) = $([HCHO]_{in}-[HCHO]_{out}) / [HCHO]_{in} \times 100\%$

where $[HCHO]_{in}$ and $[HCHO]_{out}$ were the inlet HCHO concentration and outlet concentrations at any time during the catalytic process, respectively.

2.4 Computational Details

Density functional theory (DFT) calculations were performed with DMol3 software package [34]. The optimization and energy were calculated with Perdew-Burke-Ernzerhof (PBE) functional under polarized function (DNP) basis set. The DFT semi-core pseudopotentials (DSPPs) method was chosen as the core treatment. The Grimme's method was used for dispersion correction [35]. Global orbital cutoff was set to 5.0 Å for all atoms. The electronic spin was unrestricted. For MnO_2 structure, the (110) surface was cleaved for the unit cell (Fig. S9a), followed by establishing a (3*2) supercell and building a 25 Å vacuum layer (Fig. S9b). The k-point was set to (4*4*1) for calculations. For CNT structure, the (6,6) carbon nanotube was imported, followed by building a (1*1*3) supercell. One of the carbon atoms was replaced by nitrogen to form a NCNT model. The k-point was set to (1*1*6).

3. Results and discussion

3.1. Physico-chemical characterization of catalysts

Fig. 1 shows the SEM images of MnO_2/CNTs and MnO_2/NCNT with different contents of MnO_2. With increased amounts of MnO_2 reacting with the carrier, it was clear that the number of MnO_2 nanosheets were in-situ immobilized on the CNTs/NCNT surfaces, and resultant oxidative damages to CNTs and NCNT surface

structure were observed, according to the following redox reaction:

$$4MnO_4^- + 3C + H_2O \rightarrow 4MnO_2 + CO_3^{2-} + 2HCO_3^- \quad (1)$$

Additionally, a pleated petal shape was apparent on the surface of these nanosheets, and they were bridged together to form a porous architecture. When MnO_2 nanosheets were introduced onto nano-carbon structures, the surface of the carbon structure was initially oxidized with the reduction of permanganate ions. Specifically, from the SEM images of MnO_2/NCNT (Fig. 1d and 1e), it can be clearly seen that potassium permanganate peeled off the NCNT structure, whereas some of the nanotubes have not been oxidized and exhibited very smooth surfaces. Hence, it could be preliminarily speculated that permanganate oxidation initially occurred at the edge and defect site, and with the increased concentrations or exposure, the NCNT were gradually eroded to the central areas (Fig. 1f) [32]. By the way, the oxidation process was also observed in the SEM images of MnO_2/CNTs (Fig. 1a-c). The smooth CNTs were increasingly coated by identified MnO_2 nanosheets on the surfaces. The elemental mapping of MnO_2/NCNT is shown in Fig. 1g. The Mn and O were uniformly dispersed on the shell, while C and N were present in a fair dispersion degree as along with Mn and O, suggesting the existence of NCNT.

All TEM images of MnO_2/CNT and MnO_2/NCNT composites displayed excellent hollow tubular structure with an average external diameter ranging from 15 to 45 nm and inner diameter from 6 to 25 nm (Fig. 2). The surfaces were well-covered by highly dispersed burrs. These were attributable to multiple layers of MnO_2, which formed adherent flakes by depositing onto surface defects caused by permanganate oxidation. Correspondingly, the amount of MnO_2 deposited increased with increased oxidation of the CNTs (Fig. 2b, f and j). MnO_2 nanosheets were also highly dispersed on the surface of single CNTs (Fig. 2b). The high-resolution transmission electron microscopy (HRTEM) image of 40% MnO_2/CNTs (Fig. 2g) clearly indicated lattice planes of CNTs with a spacing of 0.72 nm, and ε-MnO_2 with a spacing of 0.29 nm, which corresponds to the (100) diffraction plane. In addition, a broad and diffused halo ring pattern was observed (Fig. 2h) from the selective area electron diffraction (SAED), confirming the

presence of amorphous MnO_2. MnO_2/NCNT and MnO_2/CNTs were difficult to differentiate physical appearance as both had a similar external morphology (Fig. 2a). Nevertheless, bamboo-like structure with openings on both ends could be observed in NCNT by the successful doping of nitrogen (Fig. S2). According to the previous report, the NCNT-based composites had a wrinkled texture and relatively high defect density, which could be helpful in the acceleration of VOC oxidation [36]. This was evident in Fig. 2e, which showed a single NCNT completely encapsulated by MnO_2 nanosheets. Thus, it demonstrated that the NCNT provided an excellent surface for in-situ growth of MnO_2 nanosheets and could prevent agglomeration of the particles. Interestingly, other NCNT around the completely oxidized one did not yet start to be eroded. On the basis of these results, it could be inferred that NCNT oxidation initially occurred at defect sites and then rapidly covered the entire carbon tube, which were in coincidence with the previous SEM observations. Additionally, imperceptible lattice fringe was observed in the HRTEM image of 40% MnO_2/NCNT (Fig. 2i) further confirmed the presence of an amorphous phase of MnO_2 in the nanosheets. All the results above demonstrated successful anchoring of MnO_2 nanocomposite on the surface of the NCNT.

The X-ray diffraction patterns of MnO_2/CNT powders are shown in Fig. 3a. For carbon nanotubes with different MnO_2 content, five characteristic diffraction peaks were evident at 25.97°, 37.11°, 42.81°, 65.70°, and 78.06°. The wider diffraction peak at 25.97° and the small diffraction peak at 65.70° were indicative of the graphite structure of CNT (JCPDS 41-1487) [37]. With greater oxidation of CNTs and increased MnO_2 loading, the intensity of the primary peak for graphite structure (25.97°) decreased significantly. Peaks at 37.11°, 42.81° and 65.70° were attributed to (100), (101), (110) crystal faces of MnO_2 (JCPDS 30-0820) [25], respectively. These diffraction peaks were wide and weak, indicating an abundance of amorphous MnO_2. Generally, this might be explained as the MnO_2 present on the surface of catalyst was below the lower limit of X-ray detection, or that amorphous MnO_2 might exist in amorphous state with good degree of dispersion. In comparison to the former reason,

the latter explanation was more relevant for this research based on the obtained TEM and SAED information. The XRD diffraction patterns of MnO_2/NCNT (Fig. 3b) were very similar to that of MnO_2/CNTs. However, there was a decrease in the peak intensities of MnO_2, which indicated that the crystallinity of MnO_2 was relatively low. The diffraction peak at 25.97°on behalf of graphite structure was gradually weakened and widened because the NCNT carrier was oxidized to a greater extent and consequently the crystal structure was seriously damaged [33]. Such a phenomenon was normal for carbon nanomaterials modified with metal oxide nanoparticles, resulting in increased defects and active sites exposed for catalytic oxidation. Previous literature also showed that the combination of metal oxide nanoparticles with CNTs enhanced HCHO mineralization efficiencies [17, 42]. Moreover, these results were in good agreement with SEM, TEM and SAED results already discussed.

The pore size and distribution of MnO_2/NCNT provided important information for the catalytic process during synthesis of the material. The specific surface area (SSA) and porosity of MnO_2/CNTs and MnO_2/NCNT were analyzed by N_2 adsorption-desorption technique using BET and BJH (Barrett, Joyner, and Halenda) methods (see Table 1). Essentially, CNTs were low-dimensional nanomaterials with large SSA. After MnO_2 deposition, the SSA of CNTs initially decreased up to 40% MnO_2 loading. When the material was further oxidized, more and more MnO_2 were connected with each other to form a porous structure, and hence the SSA of the catalyst exhibited an increasing trend at 70% MnO_2 loading (Table 1). As a result of this, the average pore size and total pore volume also initially increased and then decreased. In the case of MnO_2/NCNT, the SSA and pore size distribution of NCNT and MnO_2/NCNT were also analyzed (Fig. S3). All the samples exhibited a type IV isotherm with obvious hysteresis loops at P/P_0 >0.4 in the P/P_0 range of 0.6˜1.0, suggesting the presence of a large number of mesoporous structures. In contrast to CNTs, NCNT exhibited different physical properties. With an increased MnO_2 loading, the SSA increased, but the average pore size and total pore volume gradually decreased (Table 1). In accordance with the SEM and TEM results, the inner space of NCNT was gradually exposed and more defective

sites of NCNT synchronously supplied during the oxidation process. Subsequently, a network of pores was connected to each other by the MnO_2 nanosheets and stacked into a porous skeleton architecture, which increased the SSA of NCNT. It was ascertained that the large surface area generated larger adsorption capacity for gaseous reactants, which could facilitate the catalytic conversion in the solid-gas reaction. Simultaneously, the decrease in pore size and pore volume might be due to the introduced MnO_2 nanosheets with different sizes, forming a dense accumulation of structures, leading to smaller pore size and reduced total pore volume.

The surface chemical environment and binding states of the dominant elements were characterized by XPS. The typical signals for C, N, O, and Mn were clearly presented in the full-range spectra (Fig. 4a). The C 1s spectra of different samples were shown in Fig. S4. When the spectra for MnO_2/NCNT and MnO_2/CNTs were compared, the shape and binding energy at ~284.6 eV, ~286.3 eV and ~288.2 eV were similar, corresponding to C-C, C-O and C=O bonds, respectively. However, an additional peak at 285.7 eV associated with C-N indicated successful doping of nitrogen in MnO_2/NCNT. Typically, the N 1s spectrum of MnO_2/NCNT (Fig. 4b) exhibited three main peaks at 398.3, 399.7 and 401.7 eV, which were assigned to pyridinic, pyrrolic and graphitic N [31], respectively. It was widely accepted that the presence of graphitic N contributes to improved catalytic activity for VOC oxidation in the heteroatom-doped carbon nanotubes [37].

Fig. S5 illustrates the high-resolution spectrum of Mn 2p, which was apparently divided into two peaks, attributed to Mn $2p_{3/2}$ (~ 642.2eV) and Mn $2p_{1/2}$ (~654.0 eV) with a splitting energy of 11.8 eV, proving that the Mn^{4+} ions were dominant in the catalysts. This was consistent with literature reports [38]. As observed in Fig. 4c, the Mn^{3+}/Mn^{4+} ratios were determined by their peak areas as follows: MnO_2/NCNT > MnO_2/CNTs > pure MnO_2. Generally, the oxygen vacancies increase with the ratio of Mn^{3+}/Mn^{4+}, and these were crucial as they provide the active sites for oxidation reactions [25]. Moreover, the binding energy of Mn $2p_{3/2}$ and Mn $2p_{1/2}$ peaks shifted to lower values for MnO_2/NCNT and MnO_2/CNTs compared to that of pure MnO_2 (Fig.

S5). The downshift resulted from an increase in the π electron cloud density after the indraught of carbon nanotubes, implying the presence of interfacial charge transfer from carbon nanotubes to Mn atoms [43].

Fig. 4d shows that the O1s spectrum was separated into two individual peaks at around 529.7 eV (lattice oxygen (O_{latt})) and 531.6 eV (surface oxygen species (O_{sur})). The binding energy of O_{latt} at approximately 530.0 eV was for MnO_2, and this shifted to 529.8 eV for MnO_2/CNTs and 529.7 eV for MnO_2/NCNT, respectively. It could thus be suggested that the decrease of the BE of O_{latt} was likely due to the increased electron density of O_{latt} by the existence of oxygen vacancies [30]. Furthermore, the electrophilic O_{sur} associated with the surface vacancies might play an important role in the VOCs oxidation. It was noteworthy that the O_{sur}/O_{latt} molar ratio decreased in the order of MnO_2/NCNT > MnO_2/CNTs > pure MnO_2. According to these results, we can infer that MnO_2/NCNT exhibited the best reaction activity for HCHO oxidation which was mainly attributed to the highest density of catalytically reactive sites [39].

3.2. Catalytic oxidation of formaldehyde

The HCHO removal efficiency and CO_2 selectivity of the catalysts were assessed at different temperatures (Fig. 5 and Fig. S6). The activity of the catalysts displayed a gradual increase with increasing temperature. The content of MnO_2 also had a significant influence on the catalytic activity. For MnO_2/CNTs, 40% MnO_2/CNTs exhibited the best catalytic activity at room temperature (Fig. 5a), attaining 75% of removal efficiency, and its performance below 100 °C was better than 20% MnO_2/CNTs and 70% MnO_2/CNTs. This might be due to the better electron transfer ability of the relatively complete carbon tube and the appropriate modification by MnO_2 nanosheets. When the temperature increased above 100 °C, the composite with the highest MnO_2 content (70% MnO_2/CNTs) showed the best activity with 100% HCHO removal efficiency at 150 °C, which could be ascribed to the further increase of active MnO_2 nanosheets decorated on defective sites of CNTs [27]. These results confirmed that the catalytic activity of the MnO_2/CNTs could be adjusted by turning the contents of MnO_2 nanosheets in the composite catalyst. Additionally, CO_2 selectivity measurements for

70%MnO_2/CNTs at different temperatures demonstrated that all formaldehyde was completely converted to CO_2 at 120 °C. HCHO removal efficiencies in excess of 90% were achieved for MnO_2/NCNTs at room temperature at least 15% higher than MnO_2/CNTs (Fig. 5b). In terms of CO_2 selectivity, the rising temperature greatly improved the catalytic ability to scavenge HCHO. A complete 100% conversion of HCHO to CO_2 on 40% MnO_2/NCNT was obtained at as low as 100 °C, which was about 50 °C lower than the equivalent MnO_2/CNT catalyst. Under a very high GHSV of 120,000 $mLh^{-1}g^{-1}$, the complete oxidation temperature for 40% MnO_2/NCNT was 150 °C (Fig. 5c). This was notable because it was more efficient than many metal oxides tested at lower GHSVs [31], and the similar result was observed under high HCHO concentration of 300 ppm (Fig. S7). The evaluation of catalytic stability was performed using 100 ppm formaldehyde at 30,000 mL h^{-1} g^{-1} at 100 °C. As shown in Fig. 5d, the HCHO removal efficiency and CO_2 selectivity remained above 95% with a minor fluctuation over 72 h. In addition, the apparent activation energy (E_a) was calculated according to Arrhenius plots for MnO_2/CNTs and MnO_2/NCNT, as shown in Fig. S8a (details in Supporting Information). The 40%MnO_2/NCNT showed the lower E_a value, indicating that HCHO was more easily oxidized on 40%MnO_2/NCNT. This result also revealed that the doping of nitrogen had changed the reaction mechanism compared to CNTs. Besides, the recyclability of the 40% MnO_2/NCNT was further tested for fifty successive cycles at room temperature, and the catalytic activity presented no significant difference among the cycles of use, as depicted in Fig. S8b, suggesting that the composite catalyst was able to maintain a high and stabilized conversion efficiency. As observed from Table 2, the reaction temperatures ($T_{50\%}$ and $T_{100\%}$) of the MnO_2-based catalysts could be compared for catalytic performances when their HCHO conversion reached to 50% and 100%, respectively. Note also that the catalytic performance was significantly enhanced by the recombination of MnO_2 and NCNT, which was superior to previously reported MnO_2-based catalysts. According to the catalyst characterization results, the boosted performance by MnO_2/NCNT could be due to improved electron transfer between NCNT and MnO_2. The incorporation of N-

heteroatoms would have increased the number of structural defects and valence electrons, leading to improved electron transfer and regeneration [29].

3.3. Oxygen molecule activation on CNT and NCNT

The overall HCHO oxidation by O_2 or air was generally described by the Mars-van Krevelen mechanism, as illustrated in Fig. 6a. At the first stage, the surface lattice oxygen in MnO_2 was involved into the C-H bond activation in HCHO, followed by cracking of the C-H bond and forming the surface intermediates of the adsorbed H and CO molecule. Accordingly, the lattice oxygen was transferred into CO to produce CO_2, leaving the oxygen vacancy on the MnO_2 surface. At the second stage, the activated O_2 molecule reacted with the oxygen vacancy and the adsorbed H, generating H_2O and recovering MnO_2. Herein, the NCNT was supposed to primarily enhance the oxygen activation process, thereby the overall HCHO oxidation was promoted by NCNT.

The HCHO oxidation and O_2 activation were also evaluated by DFT calculations, as shown in Fig. 6b. One of the C-H bonds in the adsorbed HCHO molecule was disrupted during the interaction with a lattice oxygen of MnO_2, producing a *CHO intermediate. The *CHO can react with another lattice oxygen atom, together with removal of hydrogen atom. Thus, the adsorbed CO_2 molecule was formed, leaving an oxygen vacancy on the surface of MnO_2. The energy evolution showed that the HCHO oxidation process involving lattice oxygen atoms (from step 1 to 5 in Fig. 6b) was an overall endothermic process. However, the energy change was not too large to overcome, so an increased temperature made it happen. The produced oxygen vacancy on MnO_2 surface would be reacted with oxygen so as to recover the catalytic activity of MnO_2.

Based on the proposed mechanism in Fig. 6 (a), the CNT and NCNT primarily influenced the oxygen activation process. As described from step 5 to 6 in Fig. 6b, the oxygen adsorptions behaved differently for CNT and NCNT. The energy of oxygen molecules was further promoted on NCNT, which was favorable for the following exergonic oxidation involving oxygen vacancy on MnO_2 (from step 6 to 7 in Fig. 6b). Besides, the difference in O-O bond length of O_2 molecules could reveal the same

conclusion that the oxygen was more active on NCNT with a 1.31 Å O-O bond, resembling an active superoxide species which would facilitate the regeneration of MnO_2. In contrast, the O_2 molecule on CNT exhibited an O-O bond of 1.23 Å, representing the inert state of oxygen.

3.4. Cost analysis

The HCHO mineralization carried out by the MnO_2/NCNT catalyst appeared to be promising, and we made a preliminary attempt to calculate the cost of the MnO_2/NCNT catalyst in this study. To date, a pilot-scale trial for HCHO removal by our synthesized catalysts was not performed, hence only the costs incurred on raw materials were considered as the major cost items in the preliminary analysis. The main raw material for MnO_2/NCNT preparation included NCNT, polyethylene glycol and $KMnO_4$, which approximately costed US$ 0.06/g, US$ 0.017/g and US$ 0.02/g, respectively. In terms of the synthetic ratio and manufacturing cost, the price of the 40%MnO_2/NCNT was about US$ 0.049/g. Compared to some noble metal catalysts, such as Au-CNT (chloroauric acid, US$ 54.74/g), Pd-CNT (palladium chloride, US$ 81.32/g), CNTs/Pt (chloroplatinic acid, US$ 52.46/g) [44], the cost of our prepared catalysts was much lower. Besides, the MnO_2/NCNT could be reused in fifty cycles without additional treatment making it a highly cost-effective catalyst during the application process (Fig. S8b). In comparison to other methods such as adsorption (US$ 0.052/g), plasma oxidation (US$ 859/m^3/h), photocatalytic degradation (US$ 378/year), which showed 20-70%, 20-60% and 10-40% removal efficiency, the catalytic oxidation process presented here was more economical with a cost reduction of 10-40% [45-49]. In terms of carbon footprint analysis, methods such as catalytic oxidation, adsorption, plasma oxidation and photocatalytic degradation were reported to respectively consume approximately 4.57×10^6, 3.21×10^2, 1.23×10^7 and 2.52×10^5 kg CO_2 equivalents [48]. Based on further experimental data, an exhaustive life cycle evaluation of the MnO_2/NCNT catalyst would be given in our future study.

4. Conclusions

In summary, N-doped carbon nanotube samples with different contents of manganese dioxide were synthesized *via* a direct *in-situ* oxidation. The morphology, crystal structure and compositional ratio of the composites, as well as their effect on HCHO decomposition at low temperature were evaluated. The formaldehyde conversion rate on MnO_2/NCNT was more than 95% at room temperature under a GHSV of 30,000 mL h^{-1} g^{-1}. When the reaction temperature was assessed to 100 °C, the formaldehyde conversion and CO_2 selectivity was 100% for 40% MnO_2/NCNT. The introduction of transition metal oxides onto NCNT carriers was more effective than that onto CNT for formaldehyde oxidation due to the synergy of well-formed interfaces and strong electron transfers. In addition, the density functional theory simulations clearly showed that the energy of oxygen molecules was further promoted on N-doped carbon nanotubes, which was favorable for the following exergonic oxidation involving the oxygen vacancy on MnO_2. This research also pointed a reliable strategy for constructing manganese dioxide/nanocarbon composites that can replace costly noble metals for the catalytic oxidation of volatile organic compounds.

Acknowledgments

This work was supported by the National Science Foundation of China (51406209); the Youth Fund of Hubei Natural Science Foundation (2019CFB212), the Guangdong Innovative Youth Talents Program, China (2018KQNCX283), the Science and Technology Program of Guangzhou, China (201704030040) and the Special Funding for the Science and Technology Innovation Team of Foshan, China (1920001000083).

Reference

[1] L. Feng, C.J. Musto, K.S. Suslick. A simple and highly sensitive colorimetric detection method for gaseous formaldehyde. J. Am. Chem. Soc. 2010, 132, 4046-4047.

[2] Q. Zhao, Y. Li, X. L. Chai, L. Z. Xu, L. F. Zhang, P. Ning, J. H. Huang, S. L. Tian. Interaction of inhalable volatile organic compounds and pulmonary surfactant: Potential hazards of VOCs exposure to lung. J Hazard Mater. 2019, 369, 512-520.

[3] Shu Y, He M, Ji J, H. B. Huang, S. W. Liu, D. Y. C. Leung. Synergetic degradation of VOCs by vacuum ultraviolet photolysis and catalytic ozonation over Mn-xCe/ZSM-5. J Hazard Mater. 2019, 364, 770-779.

[4] R. Pérez-Padilla, A. Schilmann, H. Riojas-Rodriguez. Respiratory health effects of indoor air pollution. Int. J. Tuberc. Lung. D. 2010, 14, 1079-1086.

[5] L.F. Qi, B. Cheng, J.G. Yu, W.K. Hob. High-surface area mesoporous Pt/TiO_2 hollow chains for efficient formaldehyde decomposition at ambient temperature. J. Hazard. Mater. 2016, 301, 522-530.

[6] M. Hakim, Y. Y. Broza, O. Barash, N. Peled, M. Phillips, A. Amann, H. Haick. Volatile organic compounds of lung cancer and possible biochemical pathways. Chemical Reviews. 2012, 112, 5949-5966.

[7] J. Bellat, I. Bezverkhyy, G. Weber, S. Royer, R. Averlant, J. Gi-raudon, J. Lamonier, Capture of formaldehyde by adsorption on nanoporous materials. J. Hazardous. Mater. 300 (2015) 711–717.

[8] H. X. Liu, M. Wang, J. Y. Ma, G. X. Lu. Modulation of HCHO, H_2O and H adsorption on AgPd cocatalyst by optimizing of selective exposed facet to enhancing the efficiency of conversion toxic formaldehyde into hydrogen driven by visible light. J Catal. 2019, 375, 493-506.

[9] L. Hou, X. Li, D. Xie, H. Wang. Effects of BTEX on the Removal of Acetone in a Coaxial Non-Thermal Plasma Reactor: Role Analysis of the Methyl Group. Molecules. 2018, 23, 890-904.

[10] Y. J. Wan, X. Fan, T.L. Zhu. Removal of low-concentration formaldehyde in air by DC corona discharge plasma, Chem. Eng. J. 2011, 171, 314-319.

[11] X. Fan, T. Zhu, Y. Sun, X.J. Yan. The roles of various plasma species in the plasma and plasma-catalytic removal of low-concentration formaldehyde in air. J. Hazardous Mater. 2011, 196380-196385.

[12] M.C. Hu, Z.H. Yao, X.G. Liu, L.P. Ma, Z. He, X.Q. Wang. Enhancement mechanism of hydroxyapatite for photocatalytic degradation of gaseous formaldehyde over TiO_2/hydroxyapatite. Journal of the Taiwan Institute of Chemical Engineers. 2018. 85, 91-97.

[13] Q. Yuan, Z. Wu, Y. Jin, F. Xiong, W. Huang. Surface Chemistry of Formaldehyde on Rutile

TiO_2 (110) Surface: Photocatalysis vs Thermal-Catalysis J. Phys. Chem. C. 2014, 118, 20420-20428.

[14] N. S. Kovalevskiy, M. N. Lyulyukin, D. S. Selishchev, D. V. Kozlovab. Analysis of air photocatalytic purification using a total hazard index: Effect of the composite TiO_2/zeolite photocatalyst. J. Hazard. Mater. 2018, 358, 302-309.

[15] A. A. Assadi, S. Loganathan S, P. N. Tri, S. G. Ghaida, A. Bouzaza, A. N. Tuand, D. Wolbert. Pilot scale degradation of mono and multi volatile organic compounds by surface discharge plasma/TiO_2 reactor: Investigation of competition and synergism. J. Hazard. Mater. 2018, 357, 305-313.

[16] C.H. Zhang, C. Wang, S. Gil, A. Boreave, L. Retailleau, Y.G. Guo, J.L. Valverde, A.G. Fendler. Catalytic oxidation of 1,2-dichloropropane over supported LaMnOx oxides catalysts. Appl. Catal. B. Environ, 2017, 201, 552-560.

[17] Y.Y. Wang, C.J. Jiang, Y. Le, B. Cheng, J.G. Yu. Hierarchical honeycomb-like Pt/NiFe-LDH/rGO nanocomposite with excellent formaldehyde decomposition activity. Chem. Eng. J. 2019, 365, 378-388.

[18] L. Wang, H.Q. Yue, Z.L. Hua, H.Y. Wang, X.B. Li, L.C. Li. Highly active Pt/NaxTiO2 catalyst for low temperature formaldehyde decomposition. Appl. Catal. B. Environ. 2017, 219, 301-313.

[19] L. Yu, R. S. Peng, L. M. Chen, M. L. Fu, J. L. Wu, D. Q. Ye. Ag supported on CeO_2 with different morphologies for the catalytic oxidation of HCHO. Chem. Eng. J. 2018, 334, 2480-2487.

[20] B.Y. Bai, Q. Qiao, J.H. Li, J.M. Hao, Progress in research on catalysts for catalytic oxidation of formaldehyde. Chinese. J. Catal. 2016, 37, 102-122.

[21] Z.X. Yan, Z.H. Xu, J. G. Yu, M. Jaroniec. Highly active mesoporous ferrihydrite supported Pt catalyst for formaldehyde removal at room temperature. Environ. Sci. Technol. 2015, 49, 6637-6644.

[22] H.Y. Tan, J. Wang, S.Z. Yu, K.B. Zhou. Support Morphology-dependent catalytic activity of Pd/CeO_2 for formaldehyde oxidation. Environ. Sci. Technol. 2015, 49, 8675-8682.

[23] B. Liu, Y. Liu, C. Li, W. Hu, P. Jing, Q. Wang, J. Zhang. Three-dimensionally ordered

497 macroporous Au/CeO_2-Co_3O_4 catalysts with nanoporous walls for enhanced catalytic oxidation
498 of formaldehyde. Appl. Catal. B. Environ. 2012, 127, 65-76.
499 [24] L. Ma, D.S. Wang, J.H. Li, B.Y. Bai, L.X. Fu, Y.D Li. Ag/CeO_2 nanospheres: efficient catalysts
500 for formaldehyde oxidation. Appl. Catal. B. Environ. 2014, 148-149, 36-43.
501 [25] B.Y. Bai, J.H Li, J.M Hao. 1D-MnO_2, 2D-MnO_2 and 3D-MnO_2 for low-temperature oxidation
502 of ethanol. Appl. Catal. B. Environ. 2015, 164, 241-250.
503 [26] Y.S. Xia, H.X. Dai, L. Zhang, J.G. Deng, H. He, C.T. Au. Ultrasound-assisted nanocasting
504 fabrication and excellent catalytic performance of three-dimensionally ordered mesoporous
505 chromia for the combustion of formaldehyde, acetone, and methanol. Appl. Catal. B. Environ.
506 2010, 100, 229-237.
507 [27] Y. Sekine. Oxidative decomposition of formaldehyde by metal oxides at room temperature.
508 Atmos. Environ. 2002, 36, 5543-5547.
509 [28] A.A. Balandin, Thermal properties of graphene and nanostructured carbon materials. Nat.
510 Mater. 2011, 10, 569-581.
511 [29] S.L. Candelaria, Y. Shao, W. Zhou, X. Li, J. Xiao, J.G. Zhang, Y. Wang, J. Liu, J. Li, G. Cao,
512 Nanostructured carbon for energy storage and conversion. Nano Energy. 2012, 1, 195-220.
513 [30] Y. H. Cao, h. Yu H, F. Peng, H. J. Wang. Selective allylic oxidation of cyclohexene catalyzed
514 by nitrogen-doped carbon nanotubes. ACS Catal. 2014, 4, 1617-1625.
515 [31] Q. Cao, J.A. Rogers. Ultrathin films of single-walled carbon nanotubes for electronics and
516 sensors: a review of fundamental and applied aspects. Adv. Mater. 2010, 21, 29-53.
517 [32] H. N. Jia, Y. F. Cai, X. H. Zheng, J. H. Lin, H. Y. Liang, J. L Qi, J. Cao, J. C. Feng, W. D. Feng.
518 Mesostructured Carbon Nanotube-on-MnO_2 Nanosheet Composite for High-Performance
519 Supercapacitors. ACS Appl. Mater. Inter. 2018, 10, 38963-38969.
520 [33] D. Méhn, A. Fonseca, G. Bister, J.B. Nagy. A comparison of different preparation methods of
521 Fe/Mo/Al_2O_3 sol–gel catalyst for synthesis of single wall carbon nanotubes. Chem. Phys. Lett.
522 2004, 393, 378-384.
523 [34] B. Delley. From molecules to solids with the DMol3 approach. J. Chem. Phys. 2000, 113, 7756-
524 7764.
525 [35] S. Grimme. Semiempirical GGA−type density functional constructed with a long−range

526 dispersion correction. J. Comput. Chem. 2006, 27, 1787-1799.
527 [36] A.M.P. Salvo, V. La Parola, L.F. Liotta, F. Giacalone, M. Gruttadauria. Highly loaded multi–
528 walled carbon nanotubes non–covalently modified with a bis–imidazolium salt and their use
529 as catalyst Supports. Chempluschem. 2016, 81, 471-476.
530 [37] P. X. Xiong, X. X. Zhao, Y. H. Xu. Nitrogen-Doped Carbon Nanotubes Derived from Metal–
531 Organic Frameworks for Potassium-Ion Battery Anodes. Chemsuschem, 2018, 11, 202-208.
532 [38] D.S. Yuan, J.X. Chen, J.H. Zeng, S.X. Tan. Preparation of monodisperse carbon nanospheres
533 for electrochemical capacitors. Electrochem. Commun. 2008, 10, 1067-1070.
534 [39] S. P. Rong, P. Y. Zhang, F. Liu, Y. J. Yang. Engineering crystal facet of α-MnO_2 nanowire for
535 highly efficient catalytic oxidation of carcinogenic airborne formaldehyde. ACS Catal, 2018,
536 8, 3435-3446.
537 [40] B. Bai, Q. Qiao, H. Arandiyan, J. H. Li, J. M. Hao. Three-dimensional ordered mesoporous
538 MnO_2-supported Ag nanoparticles for catalytic removal of formaldehyde. Environ. Sci.
539 Technol. 2016, 50, 2635-2640.
540 [41] W. S. Bai, F. Nie, J. B. Zheng, Q. L. Sheng. Novel silver nanoparticle–manganese
541 oxyhydroxide–graphene oxide nanocomposite prepared by modified silver mirror reaction and
542 its application for electrochemical sensing. ACS. Appl. Mater. Inter. 2014,6, 5439-5449.
543 [42] M. Saraf, K. Natarajan, S. M. Mobin. Robust nanocomposite of nitrogen-doped reduced
544 graphene oxide and MnO_2 nanorods for high-performance supercapacitors and nonenzymatic
545 peroxide sensors. ACS. Sustain. Chem. Eng. 2018, 6,10489-10504.
546 [43] J. L. Wang, J. G. Li, C. J. Jiang, P. Zhou, P. Y. Zhang. J. G. Yu. The effect of manganese vacancy
547 in birnessite-type MnO2 on room-temperature oxidation of formaldehyde in air. Appl. Catal.
548 B-Environ. 2017, 204, 147-155.
549 [44] B. H. Wu, Y. J. Kuang, X. H. Zhang, J. H. Chen. Noble metal nanoparticles/carbon nanotubes
550 nanohybrids: Synthesis and applications. Nano Today. 2011, 6, 75-90.
551 [45] H. Zaitan, A. Korrir, T. Chafik, D. Bianchi. Evaluation of the potential of volatile organic
552 compound (di-methyl benzene) removal using adsorption on natural minerals compared to
553 commercial oxides. J. Hazardous. Mater. 2013, 262, 365-376.
554 [46] S. Sultana, A. M. Vandenbroucke, C. Leys C, N. D. Geyter, R. Morent. Abatement of VOCs

555 with alternate adsorption and plasma-assisted regeneration: a review. Catalysts. 2015, 5, 718-
556 746.
557 [47] L. P. Yang, Z. Y. Liu, J. W. Shi, Y. Q. Zhang, H. Hu, W. F. Shangguan. Degradation of indoor
558 gaseous formaldehyde by hybrid VUV and TiO_2/UV processes. Sep. Purif. Technol, 2007, 54,
559 204-211.
560 [48] J. B. Wilson. Life-cycle inventory of formaldehyde-based resins used in wood composites in
561 terms of resources, emissions, energy and carbon. Wood. Fiber. Sci. 2010, 42, 125-143.
562 [49] G. C. Yin, X. W. Song, L. Tao, B. Sarkar, A. K. Sarmah, W. X. Zhang, Q. T. Lin, R. B. Xiao,
563 Q. J. Liu, H. L. Wang. Novel Fe-Mn binary oxide-biochar as an adsorbent for removing Cd (II)
564 from aqueous solutions. Chem. Eng. J, 2020, 389, 124465.
565

Figure captions

Table 1. Composition and surface characteristics of MnO_2 based catalysts.

Table 2. Comparison of MnO_2 catalytic oxidation of HCHO.

Schematic.1. Schematic illustration of MnO_2/NCNT synthesis.

Fig. 1. SEM images of 20%MnO_2/CNTs (a), 40%MnO_2/CNTs (b), and 70%MnO_2/CNTs (c); SEM image of 20%MnO_2/NCNT (d), 40%MnO_2/NCNT (e), and 70%MnO_2/NCNT (f); elemental mapping images of MnO_2/NCNT (g).

Fig. 2. TEM images of 20%MnO_2/CNTs (a), 40%MnO_2/CNTs (b), 70%MnO_2/CNTs (c), 20%MnO_2/NCNT (d), 40%MnO_2/NCNT (e), 70%MnO_2/NCNT (f); HRTEM images of 40%MnO_2/CNTs (g) and 40%MnO_2/NCNT (i); SAED pattern of 40%MnO_2/CNTs (h).

Fig. 3. XRD patterns of (a) MnO_2/CNTs and (b) MnO_2/NCNT with different MnO_2 contents.

Fig. 4. XPS spectra of MnO_2/NCNT, MnO_2/CNTs, and pure MnO_2: (a) survey spectra, (b) N 1s, (c) Mn $2p_{3/2}$, and (d) O 1s.

Fig. 5. Formaldehyde removal efficiencies and CO_2 selectivity of (a) MnO_2/CNTs catalyst and (b) MnO_2/NCNTs exposed to 100ppm HCHO and GHSV 30000 mL h^{-1} g^{-1} (c) Temperature dependence of HCHO conversion over 40% MnO_2/NCNT under the different GHSVs (HCHO concentration = 100 ppm) (d) Catalytic stability of 40%MnO_2/NCNT under 100 °C for 72 h.

Fig.6. (a) Proposed formaldehyde oxidation mechanism on MnO_2-CNTs/NCNT. (b) Catalytic cycle of formaldehyde oxidation on MnO_2-based on DFT calculations and the oxygen molecule activation on CNT and NCNT. Where red = O, white = H, grey = C, blue = N and purple = Mn.

589 Table 1. Composition and surface characteristics of MnO_2 based catalysts.

Sample	Mn (wt%)[a]	SSA(m^2 g^{-1})	Average pore size(nm)	V_{total} (cm^3g^{-1})
CNTs	—	149.29	5.45	0.201
20%MnO_2/CNTs	12.51	140.34	6.16	0.208
40%MnO_2/CNTs	25.20	132.28	6.73	0.618
70%MnO_2/CNTs	43.12	136.32	5.63	0.469
NCNT	—	68.92	7.12	0.355
20%MnO_2/NCNT	12.49	75.89	6.94	0.348
40%MnO_2/NCNT	25.17	85.52	6.54	0.288
70%MnO_2/NCNT	42.80	99.41	6.25	0.275

590 [a]: Determined by inductively coupled plasma optical emission spectroscopy (ICP-OES)
591

592 Table 2. Comparison of MnO_2 catalytic oxidation of HCHO.

Catalyst	Reaction conditions	$T_{50\%}$ (°C)	$T_{100\%}$ (°C)	References
MnO_x-CeO_2	580 ppm HCHO, GHSV~30,000 mL h^{-1} g^{-1}	>80	100	40
MnO_2/TiO_2	50 ppm HCHO, GHSV~30,000 mL h^{-1} g^{-1}	>60	130	41
Pyrolusite	400 ppm HCHO, GHSV~18,000 mL h^{-1} g^{-1}	150	180	42
α-MnO_2 nanowires	100 ppm HCHO, GHSV~90,000 mL h^{-1} g^{-1}	125	150	39
Birnessite	40 ppm HCHO, GHSV~120,000 mL h^{-1} g^{-1}	53	96	43
70%MnO_2/CNTs	100 ppm HCHO, GHSV~30,000 mL h^{-1} g^{-1}	<30	150	This study
40%MnO_2/NCNT	100 ppm HCHO, GHSV~30,000 mL h^{-1} g^{-1}	<30	100	This study

593

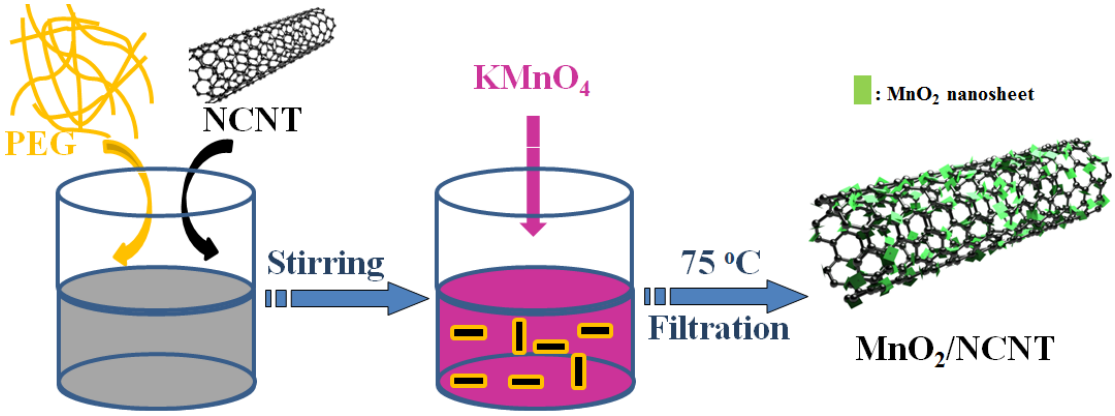

Schematic.1. Schematic illustration of MnO_2/NCNT synthesis.

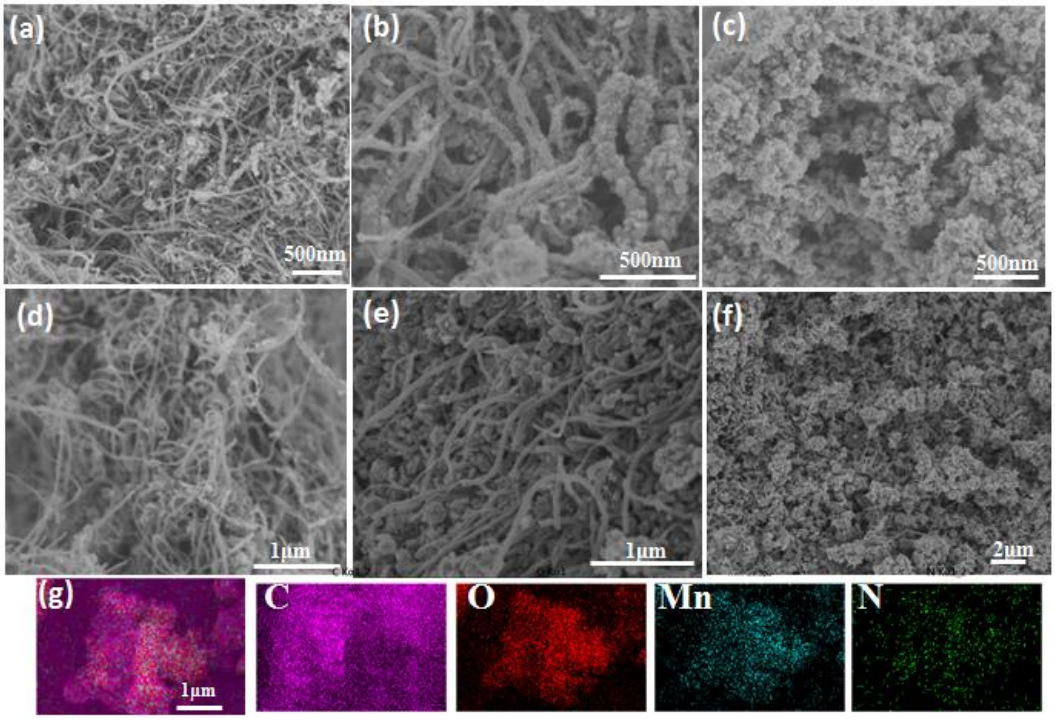

Fig. 1. SEM images of 20%MnO_2/CNTs (a), 40%MnO_2/CNTs (b), and 70%MnO_2/CNTs (c); SEM image of 20%MnO_2/NCNT (d), 40%MnO_2/NCNT (e), and 70%MnO_2/NCNT (f); elemental mapping images of MnO_2/NCNT (g).

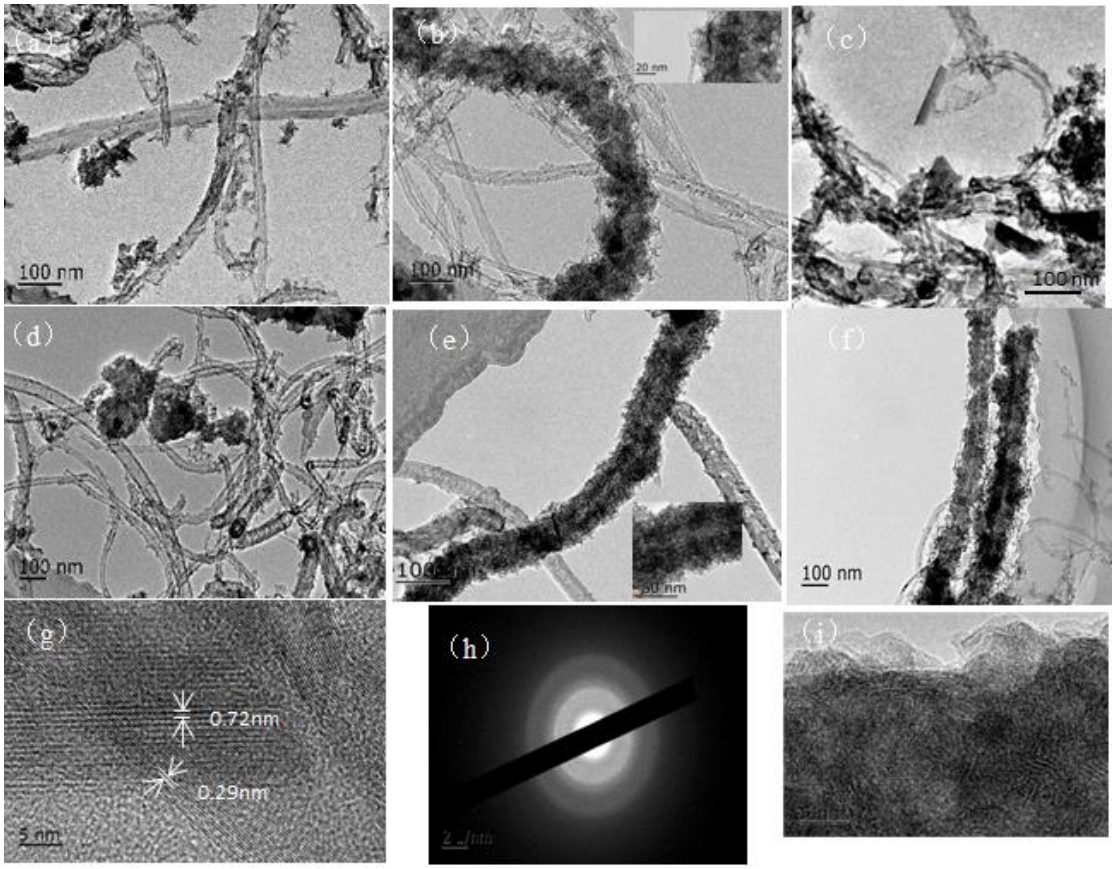

Fig. 2. TEM images of 20%MnO_2/CNTs (a), 40%MnO_2/CNTs (b), 70%MnO_2/CNTs (c), 20%MnO_2/NCNT (d), 40%MnO_2/NCNT (e), 70%MnO_2/NCNT (f); HRTEM images of 40%MnO_2/CNTs (g) and 40%MnO_2/NCNT (i); SAED pattern of 40%MnO_2/CNTs (h).

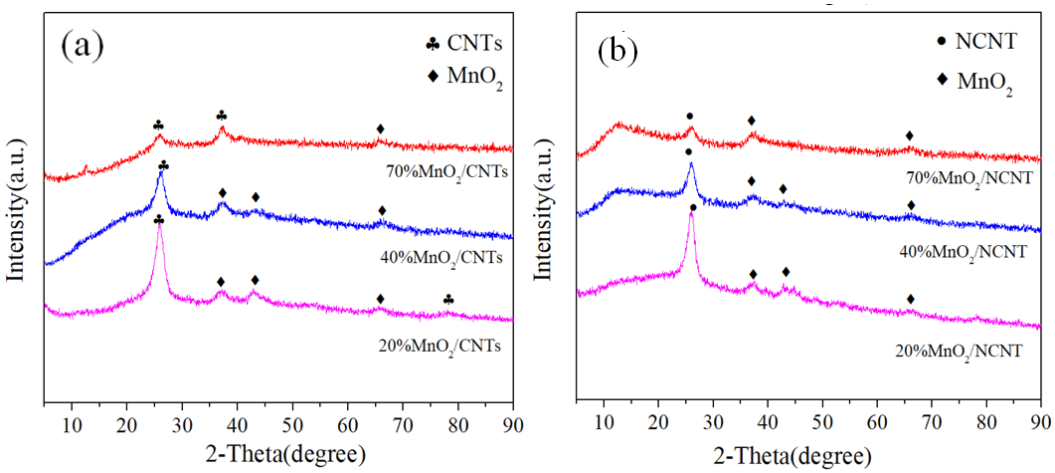

608

609 Fig. 3. XRD patterns of (a) MnO_2/CNTs and (b) MnO_2/NCNT with different MnO_2 contents.

610

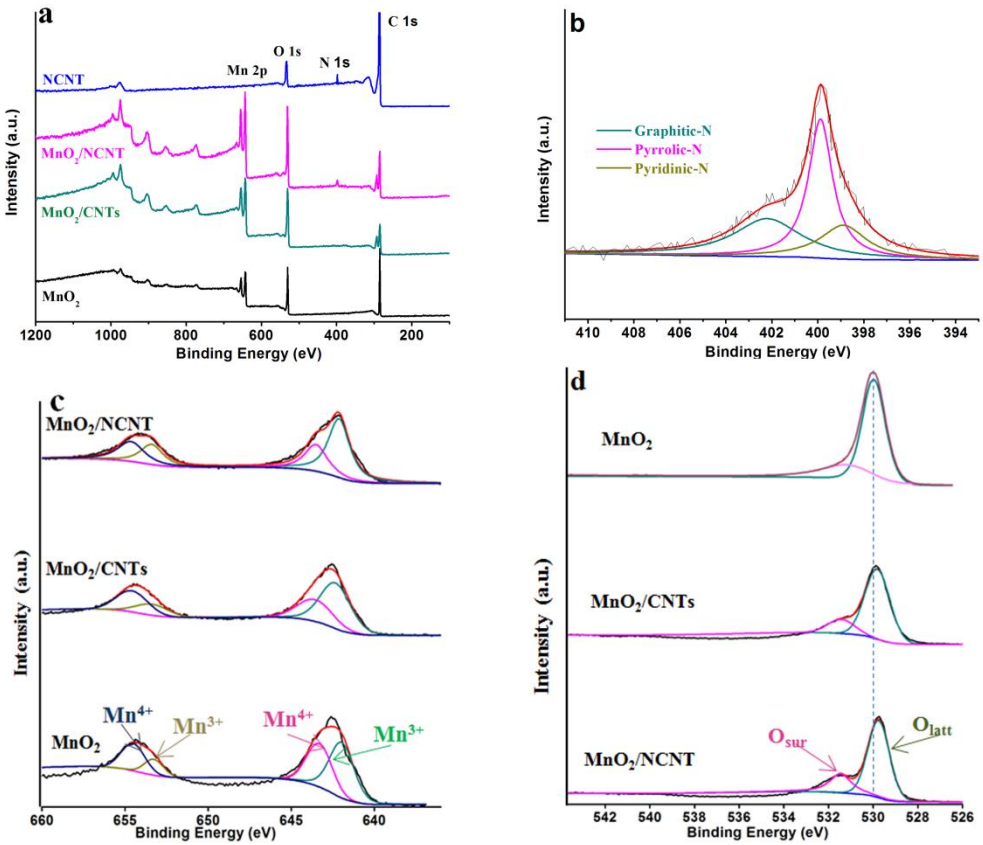

611

612 Fig. 4. XPS spectra of MnO_2/NCNT, MnO_2/CNTs, and pure MnO_2: (a) survey spectra, (b) N 1s, (c)

613 Mn $2p_{3/2}$, and (d) O 1s.

614

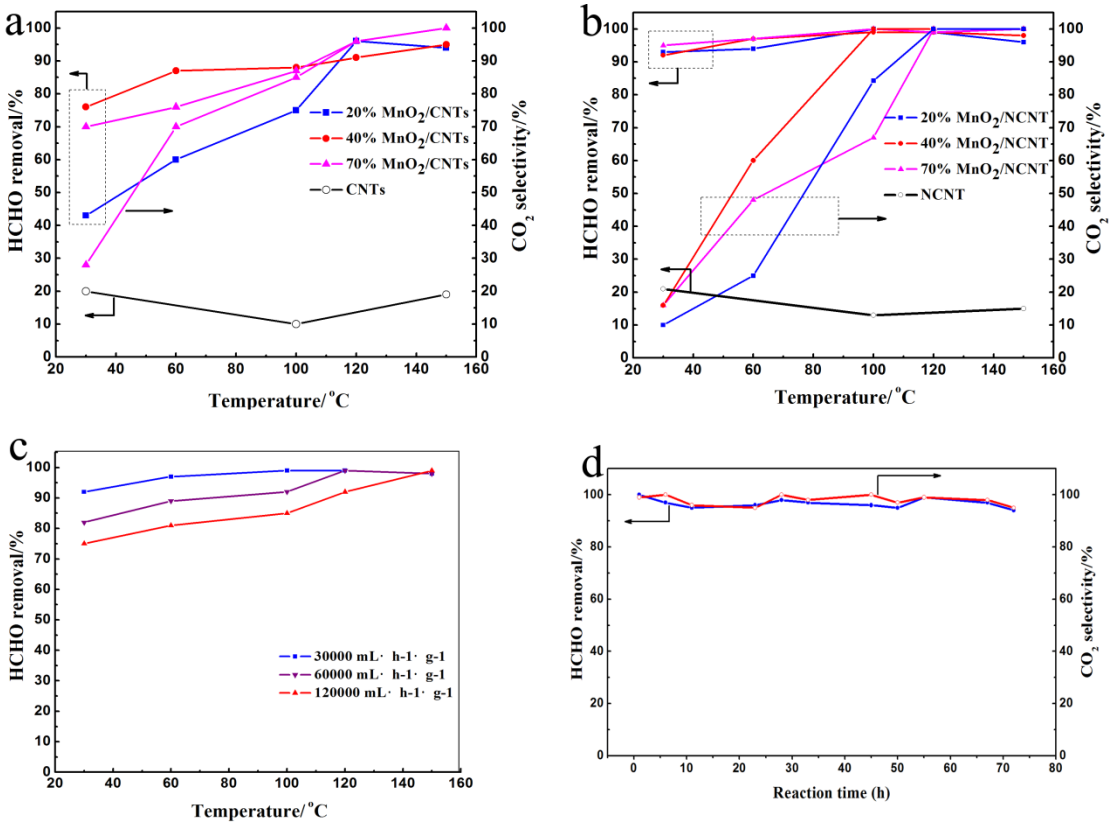

615

616 Fig. 5. Formaldehyde removal efficiencies and CO_2 selectivity of (a) MnO_2/CNTs catalyst and (b)

617 MnO_2/NCNTs exposed to 100ppm HCHO and GHSV 30000 mL h^{-1} g^{-1} (c) Temperature

618 dependence of HCHO conversion over 40% MnO_2/NCNT under the different GHSVs

619 (HCHO concentration = 100 ppm) (d) Catalytic stability of 40%MnO_2/NCNT under 100 °C

620 for 72 h.

621

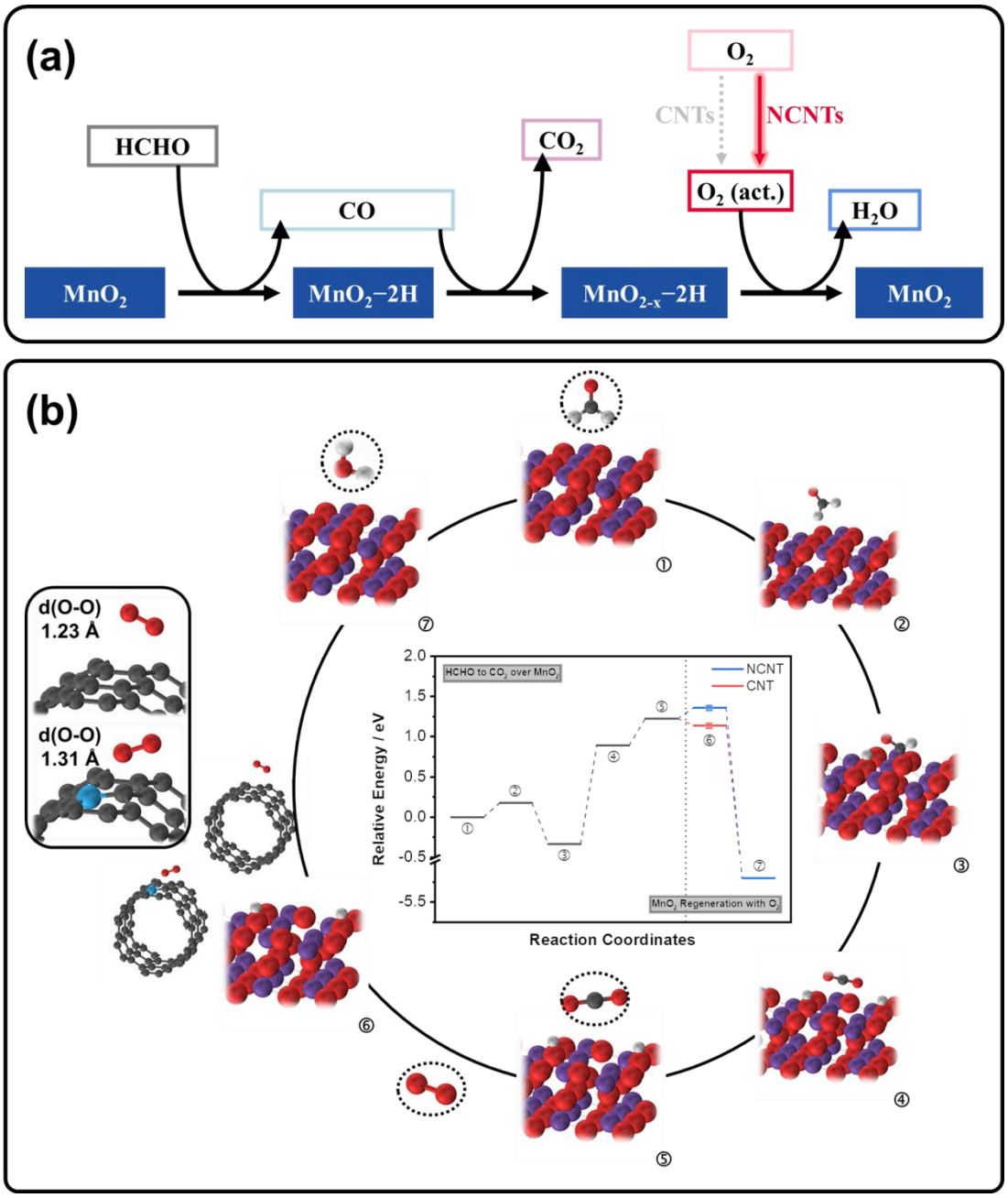

622

623 Fig.6. (a) Proposed formaldehyde oxidation mechanism on MnO_2-CNTs/NCNT. (b) Catalytic cycle
624 of formaldehyde oxidation on MnO_2-based on DFT calculations and the oxygen molecule
625 activation on CNT and NCNT. Where red = O, white = H, grey = C, blue = N and purple =
626 Mn.

627

Supporting information:

MnO_2-decorated N-doped carbon nanotube with boosted activity for low-temperature oxidation of formaldehyde

Shuai Peng[b], Xixian Yang[a*], James Strong[c], Binoy Sarkar[d], Qiang Jiang[e], Feng Peng[f], Defei Liu[a], Hailong Wang[g,h**]

[a] School of Environmental and Chemical Engineering, Foshan University, Foshan, 528000, China

[b] Hubei Provincial Engineering Laboratory for Clean Production and High Value Utilization of Bio-Based Textile Materials, Wuhan Textile University, Wuhan, 430073, China

[c] Queensland University of Technology, GPO Box 2432, 2 George St, Brisbane, QLD 4001, Australia

[d] Lancaster Environment Centre, Lancaster University, Lancaster, LA1 4YQ, UK

[e] School of Chemistry and Chemical Engineering, South China University of Technology, Guangzhou, 510000, China

[f] School of Chemistry and Chemical Engineering, Guangzhou University, Guangzhou, 510000, China

[g] Key Laboratory of Soil Contamination Bioremediation of Zhejiang Province, Zhejiang A&F University, Hangzhou, Zhejiang 311300, China

[h] Biochar Engineering Technology Research Center of Guangdong Province, Foshan University, Foshan, Guangdong 528000, China

*Corresponding authors:

Xixian Yang Email: yangxixian@yeah.net Tel/Fax: +86 757 82272751

**Corresponding author:

Hailong Wang Email: hailong.wang@fosu.edu.cn Tel/Fax: +86 757 82272751

Preparation of CNTs

Briefly, CNTs were produced by a chemical vapor deposition (CVD) method with liquefied petroleum gas as carbon source over a Fe-Mo/Al_2O_3 catalyst in a horizontal tubular quartz furnace with 4 cm inner diameter (i.d.). Before the growth of CNTs, the catalyst was activated by a mixture of H_2 and N_2 (both at 25 N cm^3 min^{-1}) for 30 min. The growth of CNTs was carried out at 700 °C for 130 min with 20 N cm^3 min^{-1} of liquefied petroleum gas, 10 N cm^3 min^{-1} of H_2, and 50 N cm^3 min^{-1} of N_2.

Static test

The static test was used to evaluate the activity of sample for HCHO removal at different temperatures (30 °C, 60 °C and 100 °C). Briefly, 100 mg of sample was put in a 3.5 L organic glass reactor. The reactor was flushed with CO_2-free synthetic air for 15 min to eliminate the interference of atmospheric CO_2 on the measurement of CO_2 formation, and the initial concentration of HCHO was adjusted to 100 ppm. The change of HCHO concentration was monitored with an Agilent 7890A online gas chromatograph with a flame ionization detector.

Calculation of apparent activation energy (E_a)

We implemented kinetics tests with both MnO_2/CNTs and MnO_2/NCNT catalysts to study the HCHO oxidation mechanism. The catalytic reaction rates at different temperatures were first obtained by assuming the first-order reaction for HCHO oxidation (it is widely accepted that the reaction for HCHO oxidation in the presence of excess oxygen follows a first-order reaction) [1-3], and then the Arrhenius plots were

obtained by plotting the logarithm of rate versus 1/T, as shown in Fig. S8a. The apparent activation energy was acquired from the Arrhenius plots.

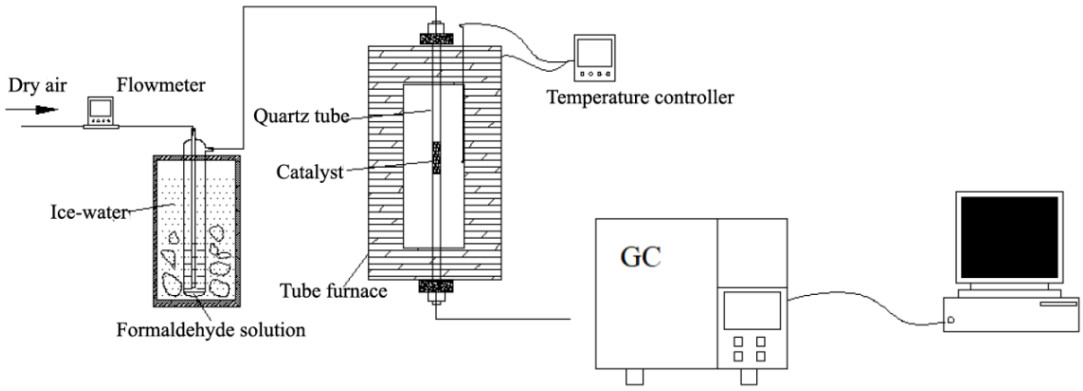

Fig. S1. Platform of catalyst activity evaluation and formaldehyde catalytic reaction

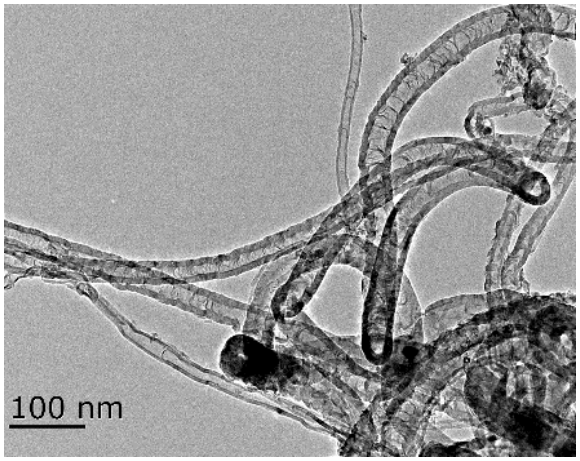

Fig. S2. TEM image of NCNT

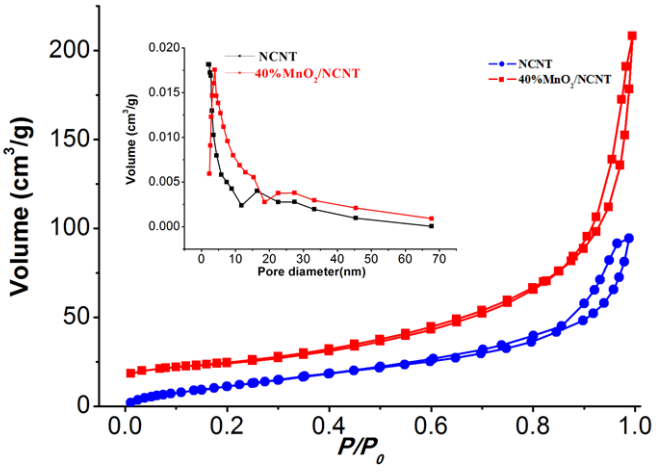

Fig. S3. N_2 adsorption-desorption isotherms and pore size distributions (inset) of the NCNT and 40%MnO_2/NCNT.

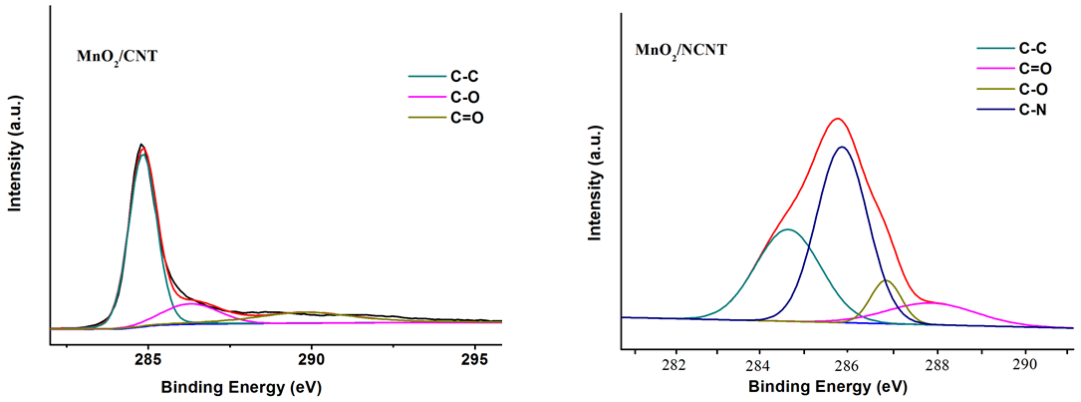

Fig. S4. C 1s XPS spectra of MnO_2/CNT and MnO_2/NCNT.

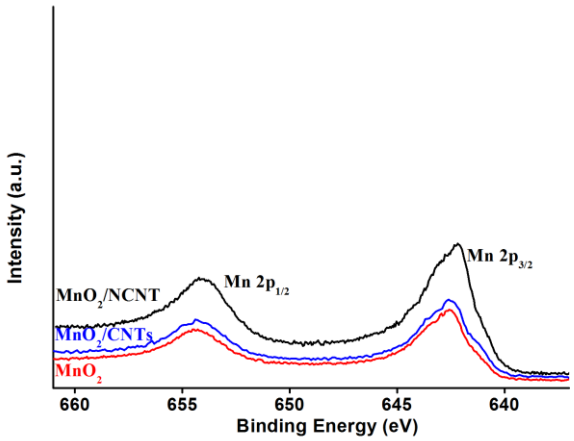

Fig. S5. Mn 2p XPS spectra of MnO_2/NCNT, MnO_2/CNTs, and pure MnO_2.

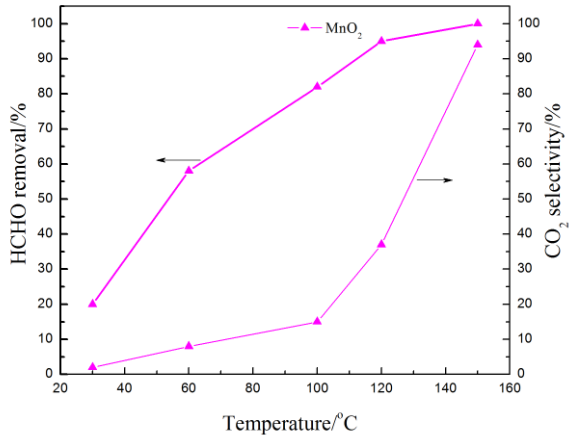

Fig. S6. Formaldehyde removal performance and CO_2 selectivity of pure MnO_2.

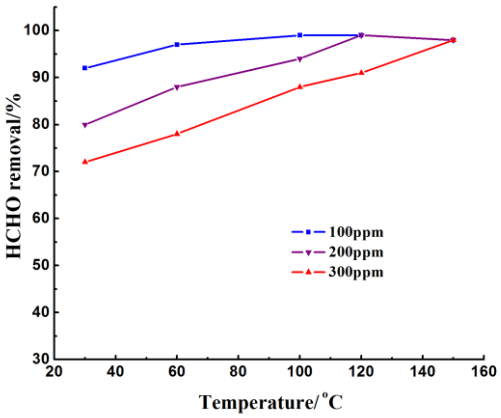

Fig. S7. Temperature dependence of HCHO conversion over 40% MnO_2/NCNT under different HCHO concentrations (GHSV = 30000 $mLh^{-1}g^{-1}$).

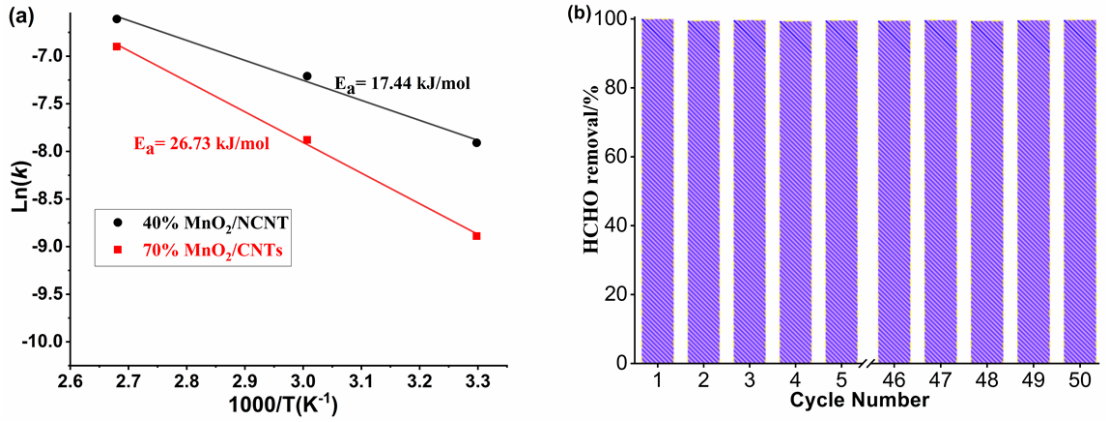

Fig. S8 (a) Arrhenius plots for HCHO oxidation over MnO_2/CNTs and MnO_2/NCNT. (b) The cycling experiments of 40% MnO_2/NCNT (HCHO concentration = 100 ppm, room temperature).

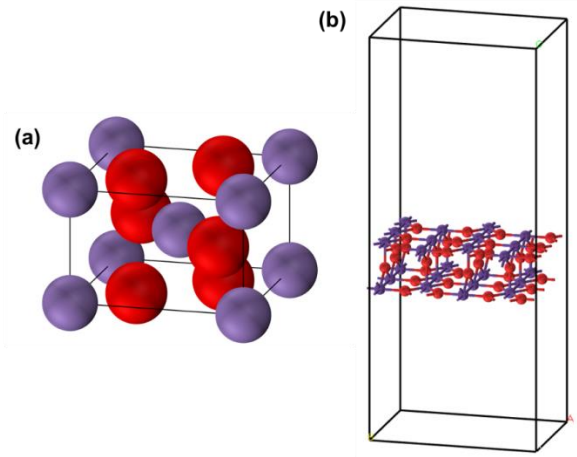

Fig. S9 (a) Unit cell of MnO_2. (b) Established (110) facet model of MnO_2 for calculations.

References

[1] Y. Wang, X. B. Zhu, M. Crocker, B. B. Chen, C. Shi. A comparative study of the catalytic oxidation of HCHO and CO over $Mn_{0.75}Co_{2.25}O_4$ catalyst: The effect of moisture. Appl. Catal. B. Environ, 2014, 160-161, 542-551.

[2] L. Lu, H. Tian, J. H. He, Q. W. Yang. Graphene-MnO_2 Hybrid Nanostructure as a New Catalyst for Formaldehyde Oxidation. J. Phys. Chem. C, 2016, 120, 23660-23668.

[3] S. P. Rong, P. Y. Zhang, F. Liu, Y. J. Yang. Engineering crystal facet of α-MnO_2 nanowire for highly efficient catalytic oxidation of carcinogenic airborne formaldehyde. ACS Catal, 2018, 8, 3435-3446.